

Transient absorption of warm dense matter created by an X-ray free-electron laser

Received: 20 December 2022

Accepted: 19 June 2024

Published online: 29 July 2024



Laurent Mercadier¹✉, Andrei Benediktovitch²✉, Špela Krušič³, Joshua J. Kas⁴, Justine Schlappa¹, Marcus Agåker^{5,6}, Robert Carley¹, Giuseppe Fazio⁷, Natalia Gerasimova¹, Young Yong Kim¹, Loïc Le Guyader¹, Giuseppe Mercurio¹, Sergii Parchenko¹, John J. Rehr⁴, Jan-Erik Rubensson⁵, Svitozar Serkez¹, Michal Stransky^{1,8}, Martin Teichmann¹, Zhong Yin^{1,10}, Matjaž Žitnik³, Andreas Scherz¹, Beata Ziaja^{2,8}✉ & Nina Rohringer^{2,9}

Warm dense matter is at the boundary between a plasma and a condensed phase and plays a role in astrophysics, planetary science and inertial confinement fusion research. However, its electronic structure and ionic structure upon irradiation with strong laser pulses remain poorly understood. Here, we use an intense and ultrafast X-ray free-electron laser pulse to simultaneously create and characterize warm dense copper using *L*-edge X-ray absorption spectroscopy over a large irradiation intensity range. Below a pulse intensity of $10^{15} \text{ W cm}^{-2}$, an absorption peak below the *L* edge appears, originating from transient depletion of the *3d* band. This peak shifts to lower energy with increasing intensity, indicating the movement of the *3d* band upon strong X-ray excitation. At higher intensities, substantial ionization and collisions lead to the transition from reverse saturable absorption to saturable absorption of the X-ray free-electron laser pulse, two nonlinear effects that hold promise for X-ray pulse-shaping. We employ theoretical calculations that combine a model based on kinetic Boltzmann equations with finite-temperature real-space density-functional theory to interpret these observations. The results can be used to benchmark non-equilibrium models of electronic structure in warm dense matter.

The transient change and control of the optical properties of matter by X-ray irradiation have led to a new area of nonlinear optical physics accessible through the development of X-ray free-electron lasers (XFELs). These sources provide intense femtosecond X-ray pulses that can drive solids out of equilibrium to induce nonlinear multiphoton effects such as saturable absorption (SA), through which, for example, a metal transiently becomes transparent in specific spectral regions^{1–4}, or its counterpart, reverse saturable absorption (RSA), during which absorption increases with increasing intensity⁵. SA occurs when the absorbing state of a material is depleted (by absorption of a high photon flux) at a faster rate than it is replenished, thus causing the absorption to saturate. RSA

occurs when the excited state of a material has a larger absorption cross section than the ground state. The temporal and spectral properties of the light pulse inducing SA or RSA undergo drastic alterations. Both effects are routinely used in the optical regime for applications such as mode-locking, pulse-shaping and two-photon microscopy^{6–8}, with possible transitions between these regimes^{9,10}. Transferring them to the X-ray spectral domain could be a route to controlled X-ray pulse-shaping^{2,11,12}. Previous studies of XFEL-irradiated matter reporting SA or RSA have mostly relied on spectrally integrated measurements^{1,3,5}. Here, we present spectrally resolved measurements of the transition from RSA to SA over a large span of applied X-ray intensities.

A full list of affiliations appears at the end of the paper. ✉ e-mail: laurent.mercadier@xfel.eu; andrei.benediktovitch@desy.de; ziaja@mail.desy.de

The solid target undergoing such intense X-ray irradiation transiently transforms into warm dense matter (WDM), a state that is too hot to be described by condensed matter physics yet too dense to be described by weakly coupled plasma physics (for a review, see, for example, ref. 13). Although there has been progress in understanding the thermodynamic and steady state structural properties of WDM in the last decade, both experimentally (for example, refs. 14,15) and theoretically (for example, ref. 16), studying the non-equilibrium electron dynamics and structural changes following an external XFEL excitation still poses great challenges. So far, X-ray emission spectroscopy has been the method of choice for revealing the evolution of XFEL-created WDM^{17–20}, estimating collisional ionization rates^{21,22} and studying the ionization potential depression^{23,24}. A complementary technique, time-resolved X-ray absorption near-edge structure spectroscopy (XANES), is a powerful tool for simultaneously probing the valence electron state and the atomic structure²⁵. Until now, XANES has mostly been applied to infrared- and optically heated WDM with picosecond to subpicosecond time resolution^{26–31}.

Here, we take advantage of the full spectral bandwidth of XFEL pulses created by the self-amplified spontaneous emission to study the formation of warm dense copper with XANES. We use a 15-fs-long XFEL pulse to excite and probe a 15-eV-wide spectral window across the Cu L_2 (952 eV) and L_3 (932 eV) edges. In both cases, direct $2p$ photoionization above the edge followed by Auger decay and electron impact ionization are the main excitation mechanisms that lead to the creation of $3d$ vacancies (Fig. 4). The latter strongly influence the overall absorption of the pulse through resonant $2p \rightarrow 3d$ transitions of several ionic species that fit into the probed spectral window. By varying the XFEL intensity, we demonstrate the transition from RSA to SA in the X-ray regime, here at the Cu L_2 and L_3 edges. Such a transition was predicted in aluminium by Cho et al.^{5,11} but has so far never been observed due to the lack of sufficient XFEL intensity. Our observations are verified by theoretical modelling of the transient absorption using Boltzmann kinetic equations to follow the evolution of the electronic configurations and high-temperature XANES calculations using the real-space Green's function code FEFF10 (ref. 32).

Spectral observations of XFEL-created WDM

Absorption spectra (see Methods for details) for a 100-nm-thick Cu film with XFEL pulses tuned to the L_3 absorption edge are shown in Fig. 1 for various pulse intensities I . For intensities $I \geq 1 \times 10^{13} \text{ W cm}^{-2}$, the absorption increases in the spectral region below the edge. This pre-edge peak is well known^{25,28–31} and is due to $3d$ vacancies, which trigger photoabsorption through $2p_{3/2} \rightarrow 3d$ transitions. The pre-edge absorption drastically increases with pulse intensity to become 2.5 times larger than the cold L_3 edge amplitude at $I_{\text{tr}} = 1 \times 10^{15} \text{ W cm}^{-2}$. This increase is accompanied by a shift of the maximum of the peak towards lower energies (redshift) due to screening effects, which are discussed in detail later. For intensities $I > I_{\text{tr}}$, further ionization broadens and shifts the spectrum maximum to higher energy (blueshift) due to reduced screening of the nuclear charge, as discussed below. The overall absorption then decreases. At the highest pulse intensity, the L_3 edge cannot be clearly resolved. A moderate, monotonic increase of absorption with photon energy is observed across the entire energy range probed.

Another distinct feature of the spectrum is an ~1-eV-wide peak centred at 936.7 eV, as indicated by the black arrow in Fig. 1. This peak is a signature of a van Hove singularity in the density of states of the face-centred cubic crystalline phase of copper, which reflects the long-range crystalline order^{33,34}. It has been shown to disappear upon melting in an optically excited pump–probe experiment³⁰, which indicates the loss of crystal order^{25,34}. In our case, the pulse duration of 15 fs is so short that no structural change involving ion motion takes place, an assumption corroborated by our observation of the van Hove peak up to intensities of $1 \times 10^{14} \text{ W cm}^{-2}$. At higher intensities, the peak is

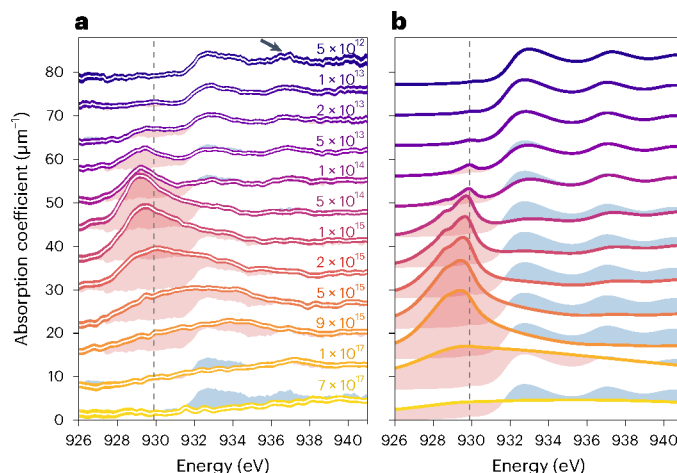


Fig. 1 | Transient XANES of XFEL-created warm dense copper. **a**, Experimental absorption spectra of 100-nm-thick film at the L_3 edge are shown for various XFEL intensities, as indicated in the figure, in W cm^{-2} . The spectra are vertically offset by $7 \mu\text{m}^{-1}$. The coloured areas around each spectrum indicate the 95% confidence intervals. The red (blue) areas show the stronger (weaker) absorption relative to the cold spectrum obtained at $I = 5 \times 10^{12} \text{ W cm}^{-2}$. The dashed line indicates the position of the pre-edge peak at low intensity. The arrow shows the characteristic peak originating from the zero-temperature van Hove singularity density of states of Cu. **b**, Corresponding theoretical XANES calculations as discussed in the text.

suppressed by several broadening mechanisms and becomes buried in the spectral region of the shifting pre-edge feature. The redistribution of the electronic states is then so strong (see discussions below) that the van Hove singularity of cold copper is no longer reliable for analysing the crystalline structure. At the highest intensity of $7 \times 10^{17} \text{ W cm}^{-2}$, the peak has disappeared.

We also measured a series of spectra at the L_2 edge (Supplementary Fig. 2). The L_2 and L_3 edges have similar structures³⁴ with an energy shift of 20 eV, but their intensities differ by a factor of 2 (the statistical branching ratio). The observed trends are summarized in Fig. 2a, in which the variations of the XFEL pulse transmission are plotted against intensity (see Methods for details). At the L_3 edge, the transmission as a function of intensity is constant up to $1.6 \times 10^{13} \text{ W cm}^{-2}$. It decreases to a minimum at a transition intensity $I_{\text{tr}} = 1 \times 10^{15} \text{ W cm}^{-2}$ and increases again for higher intensities. Similar behaviour is observed at the L_2 edge but shifted to higher intensities, with $I_{\text{tr}} = 1 \times 10^{16} \text{ W cm}^{-2}$. Looking at spectral regions centred below, on and above the L_2 and L_3 edges, we follow the spectrally resolved variation of transmission in Fig. 2b–e. A transmission minimum is observed in all regions considered except for region 1 (below the L_3 pre-edge), but the intensity at which it occurs is higher for regions with higher photon energies. These observations are discussed in detail below. Note that the transmission level below the L_3 edge at low intensity is, as expected, close to that of a cold target (87% for 100 nm; ref. 35). More measurements of the 500-nm-thick sample are presented in Supplementary Information Section II.

Theoretical description of XFEL-created WDM

Modelling the XANES structure of WDM in a state out of equilibrium is challenging. Heretofore, there has been no *ab initio* electronic structure theory capable of predicting XANES structures for the presented non-equilibrium regime. The challenge can be approached either from the plasma state or from the solid state. On the one hand, a plasma-state description can teach us about ionization dynamics, electron configurations and non-equilibrium electron energy distributions³⁶. However, it inherently lacks any description of bonding and hybridization of states and electronic bands that are crucial for XANES calculations. On the other hand, if inelastic effects are neglected, XANES structures of states under electronic equilibrium, for which an electronic temperature can

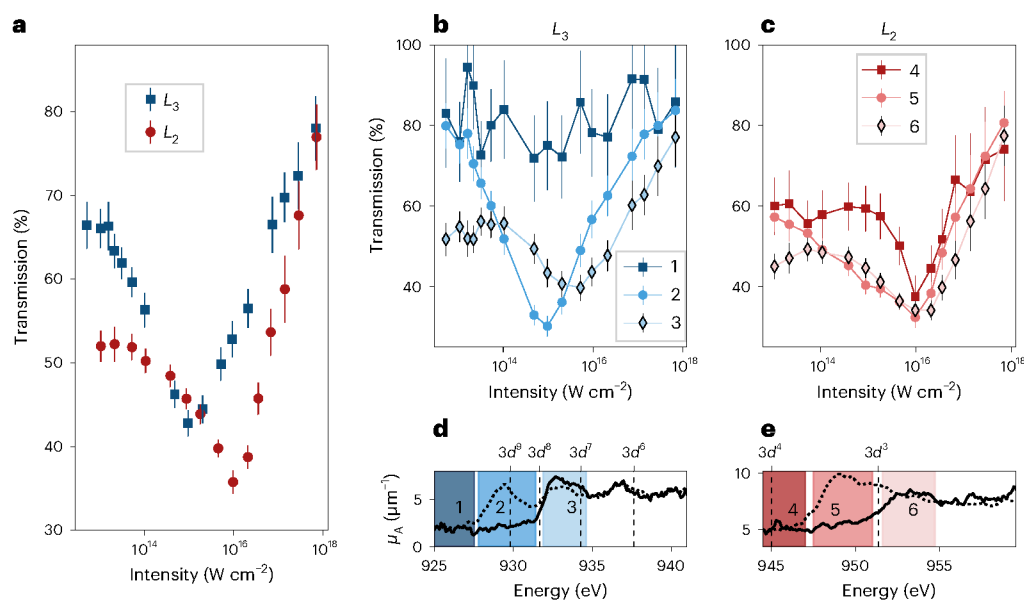


Fig. 2 | Transition from RSA to SA. a, Transmission of an XFEL pulse centred at the L_2 and L_3 edges of a 100-nm-thick Cu foil as a function of pulse intensity I . In both cases, the transmission first decreases (RSA), reaches a minimum and then increases (SA) as a function of intensity. **b, c**, Transmission at the L_3 edge (**b**) and L_2 edge (**c**) in selected spectral regions below the L_3 or L_2 pre-edge (1, 4), on the L_3 or L_2 pre-edge (2, 5) and on the L_3 or L_2 edge (3, 6), respectively, as shown

in corresponding panels **d** and **e**. **d, e**, The solid lines show the cold reference spectra (absorption coefficient μ_a) whereas the dotted lines show spectra where the pre-edge features are prominent, as obtained at $I = 5 \times 10^{13} \text{ W cm}^{-2}$ (**d**) and $I = 9 \times 10^{14} \text{ W cm}^{-2}$ (**e**). The vertical dashed lines, labelled $3d^N$, show the calculated $2p_{3/2}3d^N \rightarrow 3d^{N+1}$ excitation energies of various ions (Supplementary Information Section VI.B). The error bars in **a**, **b** and **c** indicate the 95% confidence intervals.

be defined, can be tackled by finite-temperature density-functional theory (DFT)³⁷. However, a direct extension of the principal foundations of DFT to non-equilibrium electron energy distributions has yet to be developed. Nevertheless, ad hoc extensions of DFT methods involving two non-equilibrium electronic temperatures³¹, a non-thermal lattice³⁸ or that go beyond the frozen core approximation³⁹ can be attempted for transient states of WDM out of electronic equilibrium. Moreover, finite-temperature quasiparticle approaches have recently been developed for equilibrium XANES calculations up to the WDM regime^{40,41}.

Here, we present an approach that combines a plasma description of X-ray-excited copper based on kinetic Boltzmann equations^{42–44} with finite-temperature extensions of DFT. We use the FEF10 code³² to capture the solid-state electronic structure and calculate the absorption spectrum. Briefly, the overall approach for simulating X-ray absorption is as follows. First, the Boltzmann equation solver was used to characterize the state of the system, that is, to predict the relative abundance of various atomic configurations in the system, as a function of time and XFEL intensity. Next, for each time and intensity, the FEF10 real-space multiple-scattering code was used to calculate the absorption due to each of the relevant configurations, with the surroundings approximated by atoms at the crystal lattice and with $3d$ occupation set to the average $3d$ occupation obtained from the Boltzmann model. An effective $3d$ -band temperature was introduced to fix the average $3d$ occupation within FEF10 (Supplementary Fig. 15) and allow for self-consistent relaxation of the electron density. Finally, the total absorption was calculated as an average over space and time of the contributions from all relevant configurations, weighted by the pulse intensity. Details of the theory and calculations can be found in Supplementary Information Section VI. Due to space limitations, we restrict our analysis here to a 100-nm-thick Cu film irradiated at the L_3 edge.

The Boltzmann kinetic equation solver (see Methods for details) follows the non-equilibrium evolution of emerging free-electron densities and active atomic configuration densities resulting from photoionization, Auger decays and subsequent electronic collisional processes. Detailed results obtained with the model can be found in Supplementary Figs. 9–12. The most populated Cu configurations

over the pulse duration mainly consist of various $3d$ shell occupations, although the configurations with $3p$ shell vacancies can also appear at very high intensities, as shown in Fig. 3. The model also follows the non-equilibrium evolution of the transient electron energy distribution $\rho_e(E)$, as illustrated for $I = 5 \times 10^{12} \text{ W cm}^{-2}$ and $I = 1 \times 10^{17} \text{ W cm}^{-2}$ in Fig. 4a,b, respectively. Initially, photoionization and Auger electron peaks are present in the high-energy regions of the spectra for both low and high X-ray intensities. For a low X-ray intensity (Fig. 4a), the electronic distribution below $\sim 30 \text{ eV}$ increases with time and almost stabilizes after 10 fs. It approaches a Maxwell–Boltzmann distribution, but the peak distribution in the high-energy range remains at 20 fs. This shows that the electronic system has still not equilibrated after the pulse has passed. For a high X-ray intensity (Fig. 4b), the situation is different. The peaks in the high-energy range are quickly redistributed between ~ 20 and ~ 10 fs due to efficient electron–electron interactions, which increase the overall kinetic electron energy. At 10 fs, the electron distribution has already thermalized into a Maxwell–Boltzmann distribution. The simulation thus suggests that our time-integrated XANES measurements contain notable contributions from the non-equilibrium evolution stages.

The absorption cross section at a specific instant in time and point in space depends both on the electronic configuration of the absorbing atom and on the state of the surrounding system. Absorption at the L_3 edge is simulated for each atom in the system at time t , with initial configurations taken from the Boltzmann model. In the final state of absorption, the atom has a hole in the $2p_{3/2}$ orbital. We neglect the atoms with initial configurations containing holes in deeper shells than $3d$, as their contributions are relevant only at very high intensities, $I \geq 3 \times 10^{16} \text{ W cm}^{-2}$ (Fig. 3 and Supplementary Fig. 13). The environment of the absorbing atom is accounted for by introducing an effective electronic temperature T_{eff} , chosen such that the average $3d$ -band occupation given by a self-consistent solid-state calculation matches that given by the kinetic Boltzmann simulations at time t for a given X-ray intensity. The temperature T_{eff} was found to be in good agreement with the kinetic temperature reached at the end of the pulse from Boltzmann simulations. The transient absorption cross sections

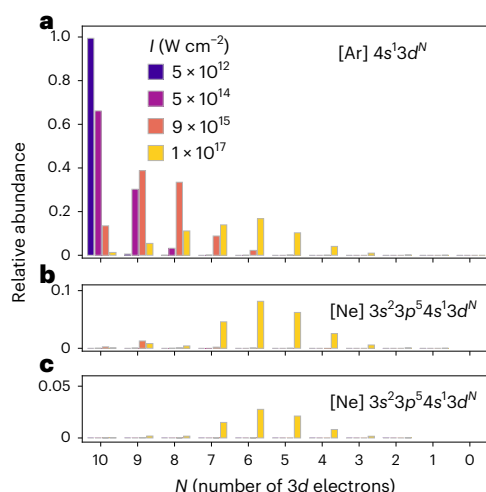


Fig. 3 | Electronic configurations of XFEL-created warm dense copper.

a–c, Relative abundances of the most populated Cu configurations averaged over the pulse duration, obtained from the kinetic Boltzmann calculations, for different pulse intensities I and plotted against the number of 3d electrons N . The base electronic configurations are [Ar] 4s¹3d^{*N*} (**a**), [Ne] 3s²3p⁵4s¹3d^{*N*} (**b**) and [Ne] 3s²3p⁵4s¹3d^{*N*} (**c**).

for each configuration λ of the absorbing atom are then calculated over a range of T_{eff} (Supplementary Fig. 19) and weighted by the relative abundances p_{λ} resulting from the Boltzmann simulations to determine the total absorption cross section $\sigma(\omega, x, y, z, t) = \sum_{\lambda} p_{\lambda}(\omega, x, y, z, t) \sigma_{\lambda}(\omega, T_{\text{eff}})$, where ω is the incoming photon frequency and (x, y, z) are the atom coordinates. To provide a gauge of the reliability of the approach, we compare it in the Supplementary Information to a second calculation that neglects the variations of the surrounding system with intensity but better accounts for the density and potential of the absorbing atom. We found that this calculation also qualitatively explains the observed trends but cannot predict the observed redshift at low to moderate intensities.

Interpretation of XANES spectra

Figure 1 compares the calculated XANES spectra to the experimental results. The theory confirms that there is a transition from RSA at low to intermediate intensities to SA at the highest intensity. RSA is evidenced by the appearance of the pre-edge peak arising from the growing probability of resonant absorption by 2p⁶3d^{*N*} atoms at low intensity. Not only does the pre-edge peak grow, but it also extends towards lower energy and shows a redshift, as in the experimental observations (Supplementary Fig. 7). Physically, several effects contribute to this net energy shift. First, the valence electron density of states (3d-DOS) is partially depopulated by the initial fraction of the pulse, starting from the most energetic electrons close to the Fermi level E_F and continuing with less energetic electrons. Consequently, as the XFEL pulse intensity is increased, the number of unoccupied 3d states probed by the remainder of the pulse increases and their average energy is reduced, as seen in Fig. 5a, which shows the redshift of the Fermi energy for different configurations. Second, as T_{eff} increases, the partial depopulation of the 3d-DOS induces a reduction of the electronic screening of the nuclear charge, which increases the electron–ion potential and leads to a dramatic redshift of the 3d band of the order of a few electronvolts to tens of electronvolts, as seen in Fig. 5b and in agreement with previous studies^{25,30,31,45,46}. However, the observed net shift is much smaller (<1 eV). This is because the reduction of the electronic screening also affects the bound (2p) electron levels by a comparable amount^{41,46}. In fact, the shift of the 2p levels dominates for highly ionized atoms and leads to blueshifted excitation energies (Fig. 2d,e and Supplementary Fig. 16).

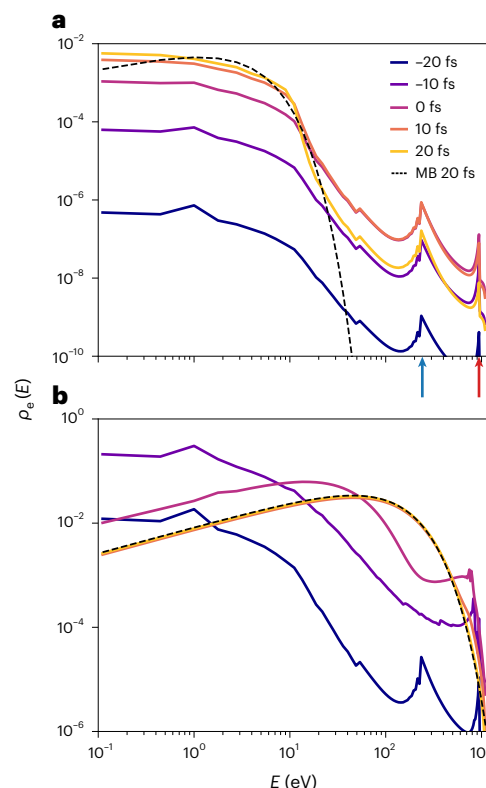


Fig. 4 | Evolution of the free-electron energy distribution. **a, b**, Evolution of the transient electron energy distribution $\rho_e(E)$ in XFEL-irradiated Cu with pulse intensity $I = 5 \times 10^{12} \text{ W cm}^{-2}$ (**a**) and pulse intensity $I = 1 \times 10^{17} \text{ W cm}^{-2}$ (**b**). The curves represent the electron distributions at various time instants with time zero corresponding to the maximum of the 15 fs FWHM Gaussian pulse. ρ_e is defined by $\int \rho_e(E) dE = \langle Z \rangle$ where $\langle Z \rangle$ denotes the transient ionization degree per atom, that is, the number of free electrons above the vacuum level divided by the total number of atoms. The black dashed curves show the Maxwell–Boltzmann (MB) distributions with a kinetic temperature equal to the average electron kinetic energy at 20 fs: 2.2 eV (**a**) and 90 eV (**b**). The broad peak with a substructure at around 250 eV, as indicated by a blue arrow, corresponds to the secondary electron emission during the collisional ionization of neutral Cu and Cu⁺ ground states. The sharp peak at 943 eV, as indicated by a red arrow, is due to the Auger decay of the 2p_{3/2} core hole.

Finally, the width of the 3d band shrinks with increasing T_{eff} (Fig. 5b). Because of this, in our calculations, the distance between the centroid of the 3d band (which is used to align the spectra) and the chemical potential for a given configuration decreases as T_{eff} is increased to produce an additional redshift for higher 3d occupation, for example, 3d⁹ and 3d¹⁰.

As the intensity is increased, we observe the continued growth, broadening and merging of this pre-edge peak with the cold edge (Fig. 1). This evolution is due to the increased probability of absorption from atoms with eight or fewer electrons in the 3d shell. These states have blueshifted excitation energies with broadened absorption profiles (Supplementary Figs. 16–18). Thus, for increasing intensity and depletion of the 3d states, the pre-edge absorption peak shifts to the blue end of the spectrum. Eventually the absorption lines move beyond the spectral window of the applied field (closing of absorption channels resulting in SA). This is why both the onset of RSA and the RSA to SA transition shift to higher intensities at higher photon energies. This can be seen in Fig. 2b,c by comparing region 2 with region 3 and region 5 with region 6. In addition, the van Hove peak decreases with intensity. Theoretical predictions indicate that it becomes negligible at $5 \times 10^{15} \text{ W cm}^{-2}$. Our experiment confirms it at $7 \times 10^{17} \text{ W cm}^{-2}$. This effect is also due to the modifications of the excited 3d band, which drastically alter the absorption spectrum for each configuration (Supplementary Fig. 17).

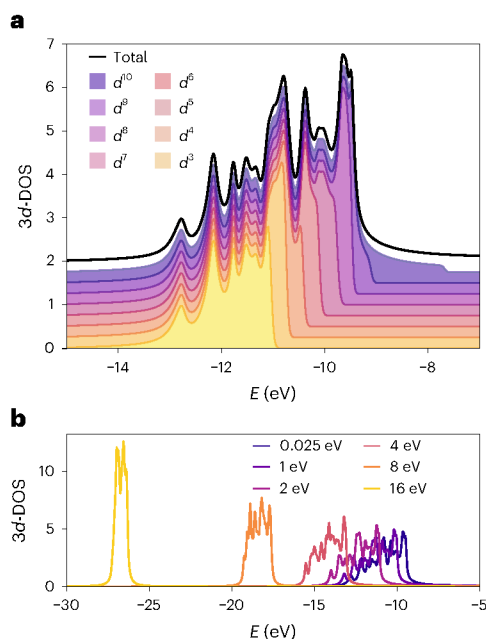


Fig. 5 | Influence of temperature on 3d-DOS. a, Occupied 3d-DOS calculated at room temperature (0.025 eV) for different configurations, which was used to find the chemical potential μ_i for each configuration. The total 3d-DOS is also shown for comparison. Similar 3d-DOS data exist for each effective temperature $T_{\text{eff}}(n)$ for each 3d-band occupancy. **b**, 3d-DOS as a function of energy relative to the vacuum level E at different effective temperatures.

Despite the overall qualitative agreement in the trends of the XANES versus pulse intensity between theory and experiment, some discrepancies are notable. In particular, the calculated RSA to SA transition occurs at higher intensity than experimentally observed. Several factors contribute to this disagreement. One is the experimental characterization of the beam intensity, which can differ by approximately 50% (Methods). Another is the restricted accuracy in the description of the state of the system by a plasma approach (here, the Boltzmann model). We discuss in detail the limitations of this model in Supplementary Information Section V.B. In addition, at low to intermediate intensities, the predicted redshift of the pre-edge peak is not as large as experimentally observed. This could be an indication that the calculation of the excitation energies is incorrect. At higher intensities, the blueshift is not seen in the peak of the theoretical spectrum. If one considers the centroid of the peak, a blueshift is evident but appears at much higher intensities than those seen in the experiment. This could again be linked to a mismatch between the relative abundance of different ionic states predicted by the Boltzmann model and that present in the real system. Another possible contribution could be an overestimate of the broadening used in the calculations. This could be due to the lack of solid-state effects in the estimate of atomic multiplet splitting, which are known to reduce the effect of e–e Coulomb interactions⁴⁷, or the use of an equilibrium distribution to describe free electrons when calculating the interaction between the photoelectron and the free electrons. One other noticeable disagreement between experiment and theory is that at intermediate to high intensities, the absorption cross section predicted by the theory at high energy (~938 to 940 eV) is reduced compared to the ambient system, whereas the experimental cross section shows little to no change. This points to the possibility that it is incorrect to use an equilibrium electron distribution when calculating the cross section.

The L_2 edge spectral region is even more complex but can be described qualitatively now that we have established the link between the blueshift of the XANES spectrum and the appearance of higher charge states. Not only does the bandwidth of the pulse contain the $2p_{1/2} \rightarrow 3d$ absorption channels of the $3d^0$ ion but also the $2p_{3/2} \rightarrow 3d$

channels of several higher ionic species, as shown in Fig. 2e. Therefore, as the pulse intensity and the ionization degree are increased, the saturation of $2p_{1/2} \rightarrow 3d$ absorption by Cu^+ is compensated for by $2p_{3/2} \rightarrow 3d$ absorption by higher charge states. This effect can be observed by comparing the evolution of spectral regions 1 and 4 in Fig. 2. Below the pre-edge absorption peak of L_3 (region 1), the transmission as a function of pulse intensity remains constant, within the measurement error. In contrast, the transmission in region 4 sharply decreases between $I = 5 \times 10^{15}$ and $1 \times 10^{16} \text{ W cm}^{-2}$. This sudden change is attributed to the opening of $2p_{3/2} \rightarrow 3d$ absorption channels in Cu^{4+} , Cu^{5+} and Cu^{6+} . These other channels contribute to the overall absorption in the L_2 spectral region. They are why the transition from RSA to SA at the L_2 edge is shifted to higher intensity compared to that at the L_3 edge.

Outlook

The experimental method presented uses averaged signal and reference spectra, but a self-referencing scheme could substantially increase the signal-to-noise ratio⁴⁸. Besides, the scheme can be extended to X-ray pump and X-ray probe XANES using the two-colour mode available at current XFEL facilities⁴⁹. This would allow us to follow the evolution of the WDM state in a time-resolved manner. Recall that the time resolution of our method is limited only by the pulse duration. The prospect of attosecond XFEL pulses and attosecond transient XANES capabilities will further widen the applicability of the presented approach in the study of matter under extreme conditions.

Online content

Any methods, additional references, Nature Portfolio reporting summaries, source data, extended data, supplementary information, acknowledgements, peer review information; details of author contributions and competing interests; and statements of data and code availability are available at <https://doi.org/10.1038/s41567-024-02587-w>.

References

- Nagler, B. et al. Turning solid aluminium transparent by intense soft X-ray photoionization. *Nat. Phys.* **5**, 693–696 (2009).
- Yoneda, H. et al. Saturable absorption of intense hard X-rays in iron. *Nat. Commun.* **5**, 5080 (2014).
- Rackstraw, D. S. et al. Saturable absorption of an X-ray free-electron-laser heated solid-density aluminum plasma. *Phys. Rev. Lett.* **114**, 015003 (2015).
- Hoffmann, L. et al. Saturable absorption of free-electron laser radiation by graphite near the carbon K-edge. *J. Phys. Chem. Lett.* **13**, 8963–8970 (2022).
- Cho, B. I. et al. Observation of reverse saturable absorption of an X-ray laser. *Phys. Rev. Lett.* **119**, 075002 (2017).
- Kärtner, F., Jung, I. & Keller, U. Soliton mode-locking with saturable absorbers. *IEEE J. Sel. Top. Quantum Electron.* **2**, 540–556 (1996).
- Wang, G., Baker-Murray, A. A. & Blau, W. J. Saturable absorption in 2D nanomaterials and related photonic devices. *Laser Photonics Rev.* **13**, 1800282 (2019).
- Kulyk, B. et al. Penta(zinc porphyrin)[60]fullerenes: strong reverse saturable absorption for optical limiting applications. *Appl. Surf. Sci.* **533**, 147468 (2020).
- Deng, X. et al. Intensity threshold in the conversion from reverse saturable absorption to saturable absorption and its application in optical limiting. *Opt. Commun.* **168**, 207–212 (1999).
- Quan, C. et al. Transition from saturable absorption to reverse saturable absorption in MoTe_2 nano-films with thickness and pump intensity. *Appl. Surf. Sci.* **457**, 115–120 (2018).
- Cho, M. S., Chung, H.-K. & Cho, B. I. Intensity-dependent resonant transmission of X-rays in solid-density aluminum plasma. *Phys. Plasmas* **25**, 053301 (2018).

12. Inoue, I. et al. Shortening X-ray pulse duration via saturable absorption. *Phys. Rev. Lett.* **127**, 163903 (2021).
13. White, T. G., Dai, J. & Riley, D. Dynamic and transient processes in warm dense matter. *Philos. Trans. R. Soc. A* **381**, 20220223 (2023).
14. Falk, K. Experimental methods for warm dense matter research. *High Power Laser Sci. Eng.* **6**, e59 (2018).
15. Riley, D. *Warm Dense Matter* (IOP Publishing, 2021).
16. Graziani, F. R., Desjarlais, M. P., Redmer, R. & Trickey, S. B. *Frontiers and Challenges in Warm Dense Matter* (Springer, 2014).
17. Vinko, S. M. et al. Creation and diagnosis of a solid-density plasma with an X-ray free-electron laser. *Nature* **482**, 59–62 (2012).
18. Vinko, S. M. X-ray free-electron laser studies of dense plasmas. *J. Plasma Phys.* **81**, 365810501 (2015).
19. Renner, O. & Rosmej, F. B. Challenges of X-ray spectroscopy in investigations of matter under extreme conditions. *Matter Radiat. Extremes* **4**, 024201 (2019).
20. Alonso-Mori, R. et al. Femtosecond electronic structure response to high intensity XFEL pulses probed by iron X-ray emission spectroscopy. *Sci. Rep.* **10**, 16837 (2020).
21. Vinko, S. M. et al. Investigation of femtosecond collisional ionization rates in a solid-density aluminium plasma. *Nat. Commun.* **6**, 6397 (2015).
22. van den Berg, Q. Y. et al. Clocking femtosecond collisional dynamics via resonant X-ray spectroscopy. *Phys. Rev. Lett.* **120**, 055002 (2018).
23. Ciricosta, O. et al. Direct measurements of the ionization potential depression in a dense plasma. *Phys. Rev. Lett.* **109**, 065002 (2012).
24. Ciricosta, O. et al. Measurements of continuum lowering in solid-density plasmas created from elements and compounds. *Nat. Commun.* **7**, 11713 (2016).
25. Dorchie, F. & Recoules, V. Non-equilibrium solid-to-plasma transition dynamics using XANES diagnostic. *Phys. Rep.* **657**, 1–26 (2016).
26. Dorchie, F. et al. Unraveling the solid-liquid-vapor phase transition dynamics at the atomic level with ultrafast X-ray absorption near-edge spectroscopy. *Phys. Rev. Lett.* **107**, 245006 (2011).
27. Cho, B. I. et al. Electronic structure of warm dense copper studied by ultrafast X-ray absorption spectroscopy. *Phys. Rev. Lett.* **106**, 167601 (2011).
28. Cho, B. I. et al. Measurement of electron-ion relaxation in warm dense copper. *Sci. Rep.* **6**, 18843 (2016).
29. B. Mahieu, B. et al. Probing warm dense matter using femtosecond X-ray absorption spectroscopy with a laser-produced betatron source. *Nat. Commun.* **9**, 3276 (2018).
30. Jourdain, N., Lecherbourg, L., Recoules, V., Renaudin, P. & Dorchie, F. Ultrafast thermal melting in nonequilibrium warm dense copper. *Phys. Rev. Lett.* **126**, 065001 (2021).
31. Lee, J.-W. et al. Investigation of nonequilibrium electronic dynamics of warm dense copper with femtosecond X-ray absorption spectroscopy. *Phys. Rev. Lett.* **127**, 175003 (2021).
32. Kas, J. J., Vila, F. D., Tan, T. S. & Rehr, J. J. Ab initio calculation of X-ray and related core-level spectroscopies: Green's function approaches. *Phys. Chem. Chem. Phys.* **24**, 13461–13473 (2022).
33. Van Hove, L. The occurrence of singularities in the elastic frequency distribution of a crystal. *Phys. Rev.* **89**, 1189–1193 (1953).
34. Jourdain, N., Recoules, V., Lecherbourg, L., Renaudin, P. & Dorchie, F. Understanding XANES spectra of two-temperature warm dense copper using ab initio simulations. *Phys. Rev. B* **101**, 125127 (2020).
35. Henke, B., Gullikson, E. & Davis, J. X-ray interactions: photoabsorption, scattering, transmission, and reflection at $E=50\text{--}30,000\text{ eV}$, $Z=1\text{--}92$. *At. Data Nucl. Data Tables* **54**, 181–342 (1993).
36. Ren, S. et al. Non-thermal evolution of dense plasmas driven by intense X-ray fields. *Commun. Phys.* **6**, 99 (2023).
37. Mermin, N. D. Thermal properties of the inhomogeneous electron gas. *Phys. Rev.* **137**, A1441–A1443 (1965).
38. Waldecker, L., Bertoni, R., Ernstorfer, R. & Vorberger, J. Electron-phonon coupling and energy flow in a simple metal beyond the two-temperature approximation. *Phys. Rev. X* **6**, 021003 (2016).
39. Zhang, Q. et al. Effect of nonequilibrium transient electronic structures on lattice stability in metals: density functional theory calculations. *Front. Phys.* **10**, 838568 (2022).
40. Tan, T. S., Kas, J. J. & Rehr, J. J. Real-space Green's function approach for X-ray spectra at high temperature. *Phys. Rev. B* **104**, 035144 (2021).
41. Tan, T. S., Kas, J. J., Trickey, S. B. & Rehr, J. J. High-temperature self-energy corrections to X-ray absorption spectra. *Phys. Rev. B* **107**, 115122 (2023).
42. Ziaja, B., Castro, A. R. D., Weckert, E. & Möller, T. Modelling dynamics of samples exposed to free-electron-laser radiation with Boltzmann equations. *Eur. Phys. J. D* **40**, 465–480 (2006).
43. Ziaja, B. et al. Kinetic Boltzmann approach adapted for modeling highly ionized matter created by X-ray irradiation of a solid. *Phys. Rev. E* **93**, 053210 (2016).
44. Ziaja, B. et al. Tracing X-ray-induced formation of warm dense gold with Boltzmann kinetic equations. *Eur. Phys. J. D* **75**, 224 (2021).
45. Bévilacqua, E., Colombier, J. P., Recoules, V. & Stoian, R. Free-electron properties of metals under ultrafast laser-induced electron-phonon nonequilibrium: a first-principles study. *Phys. Rev. B* **89**, 115117 (2014).
46. Jourdain, N., Lecherbourg, L., Recoules, V., Renaudin, P. & Dorchie, F. Electron-ion thermal equilibration dynamics in femtosecond heated warm dense copper. *Phys. Rev. B* **97**, 075148 (2018).
47. de Groot, F. & Kotani, A. *Core Level Spectroscopy of Solids* 1st edn (CRC Press, 2008).
48. Harmand, M. et al. Single-shot X-ray absorption spectroscopy at X-ray free electron lasers. *Sci. Rep.* **13**, 18203 (2023).
49. Serkez, S. et al. Opportunities for two-color experiments in the soft X-ray regime at the European XFEL. *Appl. Sci.* **10**, 2728 (2020).

Publisher's note Springer Nature remains neutral with regard to jurisdictional claims in published maps and institutional affiliations.

Open Access This article is licensed under a Creative Commons Attribution 4.0 International License, which permits use, sharing, adaptation, distribution and reproduction in any medium or format, as long as you give appropriate credit to the original author(s) and the source, provide a link to the Creative Commons licence, and indicate if changes were made. The images or other third party material in this article are included in the article's Creative Commons licence, unless indicated otherwise in a credit line to the material. If material is not included in the article's Creative Commons licence and your intended use is not permitted by statutory regulation or exceeds the permitted use, you will need to obtain permission directly from the copyright holder. To view a copy of this licence, visit <http://creativecommons.org/licenses/by/4.0/>.

© The Author(s) 2024

¹European XFEL, Schenefeld, Germany. ²Center for Free-Electron Laser Science CFEL, Deutsches Elektronen-Synchrotron DESY, Hamburg, Germany.

³J. Stefan Institute, Ljubljana, Slovenia. ⁴Department of Physics, University of Washington, Seattle, WA, USA. ⁵Department of Physics and Astronomy, Uppsala University, Uppsala, Sweden. ⁶MAX IV Laboratory, Lund University, Lund, Sweden. ⁷Laboratorium für Physikalische Chemie, ETH Zürich, Zurich, Switzerland. ⁸Institute of Nuclear Physics, Polish Academy of Sciences, Krakow, Poland. ⁹Department of Physics, Universität Hamburg, Hamburg, Germany. ¹⁰Present address: International Center for Synchrotron Radiation Innovation Smart, Tohoku University, Sendai, Japan.

✉ e-mail: laurent.mercadier@xfel.eu; andrei.benediktovitch@desy.de; ziaja@mail.desy.de

Methods

Experimental set-up

The experiment was performed at the Spectroscopy and Coherent Scattering (SCS) instrument of the European XFEL (EuXFEL). The XFEL pulse energy was measured with two X-ray gas monitors, one before beam transport and the other one in the SCS instrument hutch, just upstream of the focusing optics. A gas attenuator filled with N_2 at an adjustable pressure allowed the pulse energy to be controlled. The beam was focused by Kirkpatrick–Báez mirrors. The beam size of $4\ \mu\text{m}$ full-width at half-maximum (FWHM) was characterized by a knife-edge scan. With a pulse energy of up to $2\ \text{mJ}$ measured at the SCS X-ray gas monitor, an intensity of $\sim 7 \times 10^{17}\ \text{W cm}^{-2}$ was achieved on sample. The accuracy of the intensity reached was estimated to be $\sim 25\%$ based on the uncertainty of the measurements by the X-ray gas monitors, the transmission of the Kirkpatrick–Báez mirrors and the knife-edge beam size characterization. A pulse duration of $15\ \text{fs}$ FWHM was derived from a spectral correlation analysis (see Supplementary Information for details). The irradiated sample was a 100- or 500-nm -thick copper foil supported by a nickel mesh. Great care was taken in the fabrication (by Luxel) and handling of the experimentally studied samples, and no sign of oxidation was found, as evidenced by the absence of a pre-edge peak characteristic of CuO or Cu_2O in the low-intensity limit spectra. The sample was rastered to a pristine region for every shot at the $10\ \text{Hz}$ train repetition rate of EuXFEL, and the spectra where the beam hit the mesh were discarded in the following way. As the mesh was $15\ \mu\text{m}$ thick, it fully blocked the X-ray pulse upon irradiation, even at the highest irradiation intensities. The spectra where the mesh was hit were filtered out by setting a threshold on the intensity of the integrated spectrum below which the pulse was considered to have hit the mesh. In addition, the position of the stage was recorded and corroborated with the threshold analysis. Finally, a post-mortem analysis with an optical microscope allowed us to reliably confirm the data sorting. The very few points (approximately less than 1% of the number of pulses per XANES spectrum) where a Ni mesh hit was not clear were discarded. The spectrometer⁵⁰ was placed $2.3\ \text{m}$ downstream of the interaction point and consisted of an entrance slit of $40\ \mu\text{m}$ and a grating with $1,200$ lines per mm . It had a radius of curvature of $5\ \text{m}$ in the Rowland geometry and was coupled to a CCD camera (Andor, model Newton). The energy was calibrated using the beamline monochromator⁵¹. The low-fluence limit spectra were found to be in good agreement with those in refs. 28,30. The resolving power was $E/\Delta E \approx 2,400$. To avoid saturation of the detector, the transmitted beam was attenuated by a combination of Al filters of 3.5 , 5 or $10\ \mu\text{m}$ thickness upstream of the entrance slit of the spectrometer.

Absorption spectra

Ultrashort pulses from EuXFEL were tightly focused onto a thin Cu foil. Their energy levels were tuned at the L_2 edge ($952\ \text{eV}$) or L_3 ($932\ \text{eV}$) edge, with $\sim 40\%$ of their spectral content above the edge. The total bandwidth was $\sim 0.7\%$ FWHM. The spectrum of an XFEL pulse contains randomly distributed spikes originating from the self-amplification of the spontaneous emission process, such that averaging over many shots is necessary for a meaningful comparison of spectra with and without a sample. Examples of single-shot and average spectra are shown in Supplementary Fig. 1. For each experimental condition, including the low-intensity limit, $\sim 2,000$ single-shot spectra were recorded without a sample and 200 to $1,000$ single-shot spectra recorded with a sample. The drifts of the photon energy and pulse energy between two data acquisitions were small enough to be neglected. The absorption coefficient was then calculated for each photon energy as $\mu_A = \ln(I_{\text{ref}}/I_{\text{Cu}})/d$, where I_{ref} is the averaged reference spectrum intensity, I_{Cu} is the averaged spectrum intensity with a sample and d is the sample thickness.

Transmission of the XFEL pulse

The integral over the entire bandwidth of the spectra without a sample S_{ref} or with a sample S_{Cu} is proportional to the total number of photons

of the incoming or transmitted pulse, respectively. The total transmission is, thus, $T = \langle S_{\text{Cu}} \rangle / \langle S_{\text{ref}} \rangle$, where $\langle \dots \rangle$ is the average over the number of collected spectra of a given pulse intensity. Likewise, a spectrally resolved transmission can be defined within a specific photon-energy window of the spectra.

Pre-edge shift

The energy shift of a pre-edge feature (Supplementary Fig. 7) was extracted by determining the position of the zero-crossing of the derivative of the absorption spectra smoothed using a Savitzky–Golay filter. Given the spectrometer dispersion and the error bar in the absorption spectra, the position accuracy varied from ± 0.22 to $\pm 0.11\ \text{eV}$.

Boltzmann kinetic equations

The Boltzmann kinetic equation solver models the interaction of an X-ray pulse with a bulk material. The X-ray pulse was assumed to have a temporal Gaussian profile of $15\ \text{fs}$ FWHM. It was also assumed to be monochromatic, with photon energy $\sim 1\ \text{eV}$ above the L_3 cold edge. This approximation is justified by the slow variations of the absorption cross sections below and above the edge. In Supplementary Information Section II, we discuss the differences between excitation below and above the L_3 edge. The classical Boltzmann kinetic equations originate from the reduced N -particle Liouville equations and include only single-particle phase-space densities of charge states and free electrons in the sample. The Boltzmann equation solver, originally constructed to follow the non-equilibrium evolution of finite systems (for example, atomic clusters) in ref. 42 was adapted in refs. 43,44 to study bulk materials irradiated by X-rays. To circumvent the ‘bottleneck’ due to the very high number of active configurations involved after irradiating a material with X-rays, an alternative ‘predominant excitation and relaxation path’ approach was proposed in ref. 43. Although this approach still uses true atomic configurations, it limits their number by restricting the sample relaxation to the predominant paths, as determined by the largest cross sections and transitions rates. The current scheme includes the most probable photoionization and Auger decay channels from each configuration within the path. Consistently, only the predominant collisional ionization processes (from the outermost shell of all atoms and ions considered) and the corresponding three-body recombination rates are included. The collision terms were derived by assuming that isolated atoms interact with the impact particles, and these terms were implemented within the two- and three-body Boltzmann collision integrals (for details, see, for example, refs. 52,53), with respective cross sections and rates of atomic processes induced by X-ray photons obtained with the XATOM code^{54,55} based on the Hartree–Fock–Slater scheme. Note that the Cu $2p$ level is degenerate in this framework. It has an energy of $939.11\ \text{eV}$. Therefore, a constant redshift of $6.41\ \text{eV}$ was applied to all atomic levels calculated to fit the L_3 -edge position of neutral copper ($932.7\ \text{eV}$). Impact ionization cross sections (and the respective recombination rates) were calculated with Lotz formulas⁵⁶. The short-range electron–electron scattering was modelled with the Fokker–Planck collision integral⁵³. Pauli blocking was not included, as the electron system was assumed to be classical in this model.

Data availability

Data recorded for the experiment at the European XFEL are available (ref. 57). Source data are provided with this paper. Further experimental data as well as the simulation data that support the findings of this study are available from the corresponding authors upon reasonable request.

Code availability

The kinetic Boltzmann equation solver that supports the conclusions within this paper and other findings of this study is available under a licence agreement. The licensor is Deutsches Elektronen-Synchrotron DESY, Notkestr. 85, 22607 Hamburg, Germany. Please contact the

corresponding authors for more details. The current stable version of FEF10 is available (ref. 58). The version used for these calculations was slightly modified to allow for higher temperatures and is available (ref. 59).

References

50. Nordgren, J. et al. Soft X-ray emission spectroscopy using monochromatized synchrotron radiation. *Rev. Sci. Instrum.* **60**, 1690–1696 (1989).
51. Gerasimova, N. et al. The soft X-ray monochromator at the SASE3 beamline of the European XFEL: from design to operation. *J. Synchrotron Radiat.* **29**, 1299–1308 (2022).
52. Aristov, V. V. *Direct Methods for Solving the Boltzmann Equation and Study of Nonequilibrium Flows* (Springer Dordrecht, 2001).
53. Shkarofsky, I. P., Johnston, T. W. & Bachynski, M. P. *The Particle Kinetics of Plasmas* (Addison Wesley Publishing Company, 1966).
54. Son, S.-K., Young, L. & Santra, R. Impact of hollow-atom formation on coherent X-ray scattering at high intensity. *Phys. Rev. A* **83**, 033402 (2011).
55. Jurek, Z., Son, S.-K., Ziaja, B. & Santra, R. XMDYN and XATOM: versatile simulation tools for quantitative modeling of X-ray free-electron laser induced dynamics of matter. *J. Appl. Crystallogr.* **49**, 1048–1056 (2016).
56. Lotz, W. Electron-impact ionization cross-sections for atoms up to $Z=108$. *Z. Phys. A: Hadrons Nucl.* **232**, 101–107 (1970).
57. Data recorded for the experiment at the European XFEL. *European XFEL* <https://doi.org/10.22003/XFEL.EU-DATA-002593-00> (2021).
58. Current (2024) stable version of FEF10. *GitHub times-software*. github.io/feff10/ (2024).
59. Version of FEF10 used for the present calculations. *GitHub* github.com/times-software/feff10/tree/scf_ramp (2024).

Acknowledgements

We acknowledge EuXFEL in Schenefeld, Germany, for provision of the XFEL beamtime at the SCS scientific instrument and would like to thank the staff for their assistance. We thank A. Reich, D. Hickin and G. Giovanetti for the integration of the spectrometer and C. Deiter for support with the sample scanner. We also thank R. C. Albers for

fruitful discussions. This work is partly supported by the Cluster of Excellence ‘CUI: Advanced Imaging of Matter’ (EXC 2056) of the German Research Foundation (Project ID 390715994). B.Z. and M.S. thank EuXFEL and the Institute of Nuclear Physics, Polish Academy of Sciences, in Krakow for support through a joint R&D project. J.J.K. and J.J.R. are supported by the Theory Institute for Materials and Energy Spectroscopies at SLAC, which is funded by the US Department of the Environment, Office of Basic Energy Sciences, Division of Materials Sciences and Engineering (Contract No. DE-AC02-76SF0051).

Author contributions

L.M., A.B., J.S. and N.R. conceived the experiment. L.M., A.B., S.K., J.S., M.A., R.C., G.F., N.G., Y.Y.K., L.L.G., G.M., S.P., J.-E.R., S.S., M.T., Z.Y., M.Z. and A.S. conducted the experiment at the SCS instrument of EuXFEL. A.B., B.Z., M.S., J.J.K. and J.J.R. performed the theoretical calculations. L.M., S.K. and A.B. analysed the data. L.M., A.B., B.Z., J.J.K., J.J.R. and N.R. interpreted the data and wrote the manuscript with input from all authors.

Funding

Open Access funding enabled and organized by Projekt DEAL.

Competing interests

The authors declare no competing interests.

Additional information

Supplementary information The online version contains supplementary material available at <https://doi.org/10.1038/s41567-024-02587-w>.

Correspondence and requests for materials should be addressed to Laurent Mercadier, Andrei Benediktovitch or Beata Ziaja.

Peer review information *Nature Physics* thanks Marion Harmand and the other, anonymous, reviewer(s) for their contribution to the peer review of this work.

Reprints and permissions information is available at www.nature.com/reprints.